Version of Record: https://www.sciencedirect.com/science/article/pii/S2772369022000329
Manuscript_565efaf5b17f64747d4a8938672b3ff5

Synthesis of a 316L Stainless Steel – Copper Composite by Laser Melting

Kijoon Lee [a,c], V. Vinay K. Doddapaneni [b], Saereh Mirzababaei [a,c], Somayeh Pasebani [a,c], Chih-hung Chang [b] and Brian K. Paul [a,c]

[a] School of Mechanical, Industrial and Manufacturing Engineering, Oregon State University, Corvallis, OR, 97330
[b] School of Chemical, Biological and Environmental Engineering, Oregon State University, Corvallis, OR, 97330
[c] Advanced Technology and Manufacturing Institute (ATAMI), Corvallis, OR 97330

Abstract

This paper demonstrates a laser melting method to produce a metal matrix composite with a higher thermal conductivity compared to 316L stainless steel using a jettable Cu ink. A novel canister was used to control the oxygen level during laser processing to emulate a hybrid inkjet-powder bed fusion technique for doping the stainless steel powder bed with Cu precursor ink. The thermal conductivity of the composite was found to be 187% higher than that of 316L stainless steel, while the microhardness decreased by 39%. Microstructural results show opportunities to further enhance the thermal conductivity and mechanical properties of the composite by eliminating interfacial cracking.

Keywords: Laser melting, metal matrix composite, effective thermal conductivity, austenitic stainless steel

1. Introduction

Though the propagation of heat within homogeneous solids is diffusive in nature, like electricity, heat can be guided through solid matter via the path of least resistance. Previous studies into controlling heat flow within solids have used lattice structures [1, 2] and anisotropic thermal conductivity [3-8] for demonstrating principles such as thermal cloaking and thermal focusing among others. The use of anisotropy in permeability and thermal conductivity has been proposed within metal foam heat sinks for enhancing heat transfer rates through improved fin efficiency [9]. Further, it is expected that anisotropic thermal conductivity could be helpful in minimizing parasitic losses due to axial heat conduction within compact heat exchangers [10, 11].

In terms of methods for modifying the thermal conductivity of alloys and metals, various strategies have been used. In the examples above, techniques used to implement anisotropic thermal conductivity included methods for embedding metal within silicone or lower thermal conductivity metals as well as methods for circuit board manufacturing. Other methods for enhancing the thermal conductivity of metals have included pressurized infiltration [12, 13] and powder metallurgy [14, 15]. None of these approaches are useful for scaling up directional strategies for controlling heat flux within metal components.

Using laser powder bed fusion (LPBF), metal matrix composites (MMCs) have been produced using ball-milled powders. Kenel et al. [16] demonstrated the use of scanning strategies to reduce the cracks of an oxide dispersion strengthened (ODS) γ-TiAl alloy produced via a LPBF tool using a mechanically alloyed powder. Ghayoor et al. [17] consolidated a near-fully dense ODS stainless steel (SS) alloy, possessing good thermal stability [18], via LPBF using 304L SS powder lightly mixed with yttria particles. However, none of these methods permit the selective tailoring of properties during the build cycle to enable directional properties.

More recently, Paul et al. [19] investigated a new hybrid LPBF method that used piezoelectric inkjet technology to produce an ODS 304 SS alloy made by doping yttria precursors within a 304 SS powder bed, prior to laser consolidation. This method required the development of an yttrium-nitrate precursor ink capable of being inkjetted into the powder bed. The advantage of this approach is the ability to

selectively modify material parameters within different parts of the powder bed during the build cycle, providing a means to control material properties within the build volume of the tool.

The goal of this paper is to demonstrate a laser melting method that uses a jettable Cu ink to produce a 316L SS-Cu composite with higher thermal conductivity than 316L SS. The motivation for this work is the development of a chemical reactor, using the new hybrid inkjet-LPBF technique, that can take advantage of directional thermal conductivity to reduce the overall size and weight of the reactor. The purpose of this paper is not to report on efforts to produce the reactor, rather, to demonstrate the feasibility of producing the composite material using a jettable ink. Specifically, this paper discusses the selection of the precursor Cu ink and the methods used to produce composite test articles for characterizing the density, composition, microhardness and thermal diffusivity of the material.

2. Experimental Approach

2.1. Ink selection

Among many Cu-based inks developed for electronics applications [20], two inks were selected as ink candidates based on the following criteria: oxidation stability, compatibility with an inkjet printhead, minimum or no requirement of additives, and minimum residue after conversion. The first ink was Cuf-AMP, which uses copper formate (Cuf) as copper salt and is widely studied to print conductive patterns. The salt decomposes to copper, hydrogen, and carbon dioxide around the temperature of 200 °C – 250 °C [21, 22]. The decomposition temperature can be lowered to around 185 °C by modifying Cuf with 2-amino 2-methyl 1-propanol (AMP) [20, 23, 24]. The modified salt was synthesized as reported by Shin et al [23]. 1:2 ratio of copper formate tetrahydrate (Cuf·$4H_2O$, 98%, Fisher Scientific) to AMP (99%, Acros Organics) was dissolved in methanol (MeOH, acs grade, Macron Fine Chemicals), and magnetically stirred for an hour. Then the solvent was removed by rotary vacuum evaporation followed by a vacuum furnace at 50 °C. Finally, the ink was prepared by mixing 1.2:1 precursor complex to the methanol.

$$Cu(HCOO)_2 \xrightarrow{185°C} Cu\,(s) + H_2(g) + 2CO_2\,(g) \quad (1)$$

Another precursor ink was vinyl trimethyl copper (II) hexafluoro acetylacetonate (Cu (hfac) VTMS, Gelest Inc.) which is widely used for chemical vapor deposition of copper films [25, 26]. The ink is liquid at room temperature, which can disproportionate into copper products and process gas by-products between 140 and 200 °C [27].

$$2\,Cu(hfac)VTMS \rightarrow Cu(s) + Cu(hfac)_2(g) + 2\,VTMS\,(g) \quad (2)$$

Table 1. Properties of Cu-based inks.

Precursor	Cuf-AMP	Cu (hfac) (VTMS)
Reaction temperature	140-190°C [23]	140-200°C [27]
Solvent requirement	Yes (Methanol)	No
Theoretical wt% of Cu	15-20%	10-20%
Reducing agents	Not required [22]	Not required [24]

The as-prepared Cuf-AMP-MeOH and as-purchased Cu-hfac-VTMS inks were deposited onto preheated glass substrates of 185 °C and 150 °C, respectively, by drop-casting in within a controlled atmosphere (less than 10 ppm of oxygen) of a glovebox. After conversion, both Cu films were characterized using a Rigaku Ultima IV diffractometer.

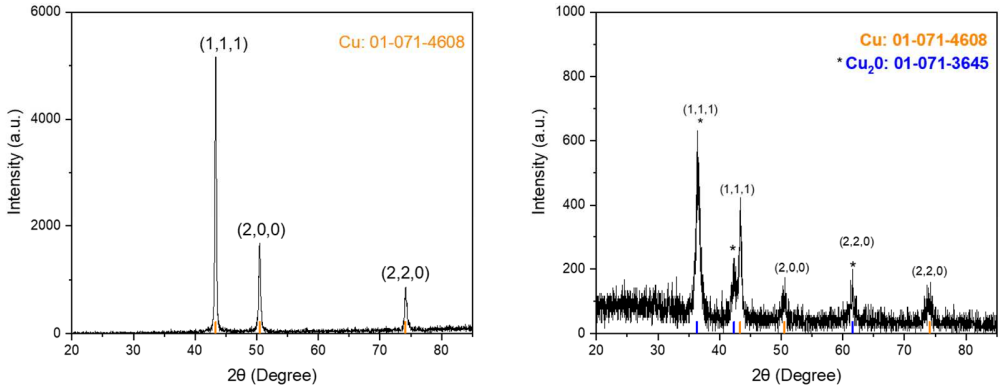

Fig. 1. XRD of converted copper films from (a) Cuf-AMP ink and (b) Cu (hfac) (VTMS) ink.

Fig. 1a shows metallic Cu peaks observed from the Cu film obtained from the converted Cuf-AMP ink. In contrast, Fig. 1b shows that both Cu and Cu_2O phases were detected from the Cu film from converted Cu (hfac) (VTMS) ink. Since copper oxides have lower thermal conductivity than copper, Cuf-AMP ink was selected as the precursor ink for fabricating the SS-Cu MMC.

2.2. Effect of ink conversion on microstructure

Use of the Cuf-AMP ink for electronics applications involves ink jetting the precursor onto a substrate before evaporating the solvent and, finally, thermally decomposing the precursor [20, 23, 28]. Adapting this ink conversion sequence to the hybrid LPBF process would involve three steps: powder layering, ink jetting and powder consolidation/precursor conversion. However, concerns arose over how much solvent would be required to reach 60 wt% copper and whether the solvent would flood the bed during deposition. Further, once the solvent was within the powder, it was anticipated that it would likely be difficult to remove. Finally, concerns existed over how the laser would interact with any residual solvent remaining in the powder bed. In particular, would flash evaporation of the solvent lead to increased spattering or leave behind carbon residue? So an alternative approach was envisioned to pre-heat the powder bed prior to ink jetting so that 1) the solvent would flash evaporate upon contact with the powder bed, avoiding wicking and flooding within the powder bed; and 2) the precursor would thermally decompose prior to being consolidated with the laser.

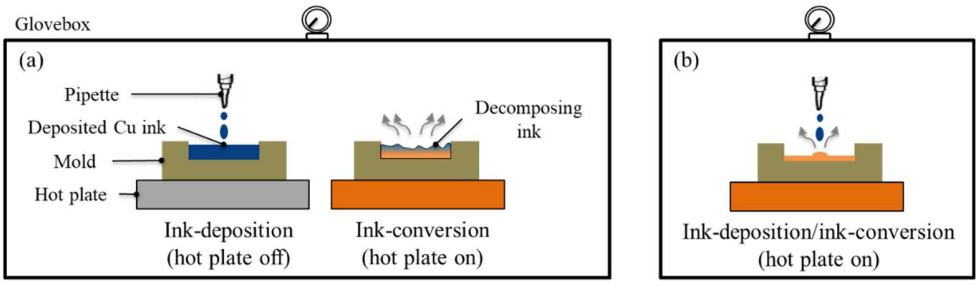

Fig. 2. Schematic diagram of (a) post-heating and (b) heated-bed methods of ink conversion.

A preliminary experiment was performed to determine whether flash evaporation and thermal decomposition of the ink led to greater contamination of the copper, due to the entrainment of chemical byproducts, than conventional drying and thermal decomposition. To determine the effect of the conversion method, two small coupons were produced using the two methods and compared in terms of microstructure.

To produce the post-heating coupon, four steps were repeated three times. To emulate the low oxygen atmosphere within the hybrid LPBF process, the first two steps were conducted within a Vacuum Technology Inc. universal glovebox under a controlled atmosphere of less than 10 ppm of oxygen. First, 620 µL of ink was pipetted within a 316L stainless steel (SS) mold (15 mm diameter and 1 mm thickness) used to contain the liquid. The volume of ink per layer was determined based on a desire to reach 60 wt% Cu, which was calculated using a theoretical copper conversion ratio (8 wt% Cu per ml of ink) and the amount of SS powder used per layer. Second, the mold was placed onto a hot plate to heat the mold and ink from room temperature to 185°C and held for three minutes allowing the methanol solvent to boil off and leaving the remaining precursor to decompose into copper (Fig. 2a). Third, the mold was taken out of the glovebox where 55.3 mg of Carpenter Additive gas-atomized austenitic 316L SS powder was measured out using an analytical balance (4 digit) and placed onto the converted copper. The powder was characterized using Malvern Panalytical laser diffraction particle analyzer showing a powder distribution of Dv10 = 18.7 µm, Dv50 = 30.1 µm and Dv90 = 49.1 µm. Afterwards, the mold was tapped to spread the powder uniformly on the converted Cu film, leading to a powder-on-Cu layer of around 0.06 mm thick per layer. Fourth, laser consolidation and mixing of the Cu and powder was performed within a laser canister [19], having a controlled oxygen atmosphere, which was inserted into a Rofin FL010 laser welder. The canister permitted interaction between the sample and a 1080 nm 1000 W laser through a 6.35 mm thick quartz window. To emulate the hybrid LPBF atmosphere, the canister was purged three times by pulling the pressure down to 5 kPa and refilling with 99.999% pure argon yielding less than 10 ppm molecular oxygen. Table 2 shows the parameters used for laser consolidation. These four steps were repeated twice more to produce enough composite material within the SS mold for microstructural analysis.

Fig. 2b and Fig. 3 show the sequence of three steps used to fabricate a microstructural coupon using the heated-bed method. First, the same volume of ink (620 µL per layer) was pipetted in increments into a pre-heated (185°C) mold (same dimensions) and flash converted within the glovebox under an environment of less than 10 ppm oxygen. During pipetting, a 30 second delay was provided between every 100 µL of precursor to ensure evaporation of solvent or venting of gaseous byproducts from the conversion. This was done recognizing that the jetting of picoliter droplets of ink into the powder bed would be much slower than continuous pipetting and, therefore, provide a better means to vent byproduct gases. Consequently, the time at conversion temperature was three minutes for both samples providing the same time for driving off gaseous byproducts as with the post-heating coupon. Second, the mold was removed from the glovebox where 55.3 mg of powder was added onto the converted copper and spread out by tapping (Fig. 3a). Third, the powder and copper layer were consolidated using the parameters in Table 2 (Fig. 3b).

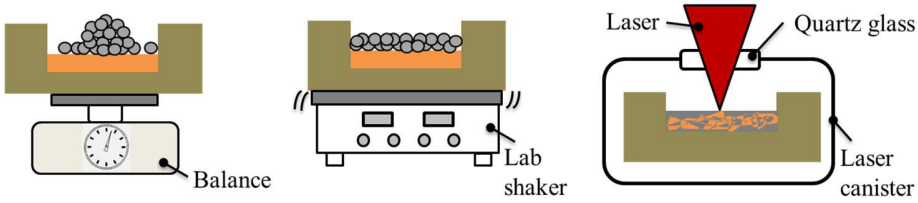

Fig. 3. Diagram of experimental setup and process steps that were repeated for fabricating the 316L SS – Cu composite coupon produced using the heated bed method.

Table 2. Process parameters of the laser consolidation.

Beam power (W)	Scan speed (mm/s)	Hatching space (µm)	Layer thickness (µm)	Approximate Cu wt%
200	150	75	60	60

After fabricating the coupons, they were cross-sectioned, polished and analyzed using an optical microscope. Prior to analyzing the cross-sections in a scanning electron microscope (SEM), the coupons were electrochemically etched using a solution of 90 wt% deionized water and 10 wt% oxalic acid with 15V DC for 5 s. The chemical composition of the samples was investigated using both energy dispersive X-ray spectroscopy (EDS) and wavelength dispersive X-ray spectroscopy (WDS). EDS analyses were conducted at 15 kV accelerating voltage and a working distance of 10.5 mm using an FEI Quanta 600F SEM. WDS analyses were performed using a CAMECA SX-100 electron microprobe (EMP) equipped with five wavelength-dispersive spectrometers and high-intensity dispersive crystals for high-sensitivity trace element analysis. The materials were analyzed using 15 keV accelerating voltage, 50 nA sample current, and 1 µm beam diameter. Counting times at the peaks were 10 s for O, Fe, Mn, Cr and Mo, 30 s for Si, Al, S, P, Cu and Ni, and 60 s for C. Data reduction was performed online using a stoichiometric PAP correction model [29]. Back-scattered electron (BSE) images were obtained using the same instrument using the CAMECA Peak Site software. Standards used for calibration were Basalt glass (USNM# 113498/1) for Si and O; Labradorite (USNM# 115900) for Al; pure C (Cameca standard) for C; Pyrite (USNM# 17024300) for S and Fe; Apatite (USNM# 104021) for P; Chalcopyrite (USNM# C558900) for Cu; Ni_2Si for Ni; pure Mn (Cameca standard) for Mn; pure Cr (Cameca standard) for Cr, and pure Mo (Cameca standard) for Mo.

2.3. Disk-shaped coupon

Based on this preliminary experiment, it was found that the heated-bed method produced better microstructures. A disk-shaped coupon for measuring the effective thermal conductivity of the composite was fabricated via the heated-bed method using the process parameters shown in Table 2. Once the MMC material was synthesized in the mold, the disk-shaped coupon was cut via wire electrical discharge machining. A diameter of 12.0 mm and thickness of 0.5 mm cylindrical coupon was used to measure the thermal diffusivity by a laser flash analyzer (LFA 457, NETZSCH, Germany). The approximate composition of the sample was determined by averaging results from EDS analyses at nine locations across the coupon.

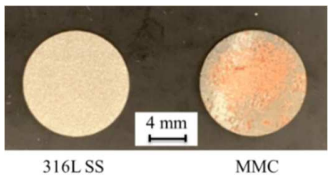

Fig. 4. Fabricated sample for laser flash analysis

Thermal conductivity, which is an intrinsic property of a material, can be derived as

$$k = \alpha \cdot \rho \cdot c_p \tag{3}$$

where k is the thermal conductivity, α is the thermal diffusivity, ρ is the density and c_p is the specific heat. Prior to measurement, the sample was coated with graphite on both sides to improve absorptivity and emissivity. The measurement was conducted at a temperature of 50 °C. The true density of the samples was measured by Archimedes' method. The porosity was estimated by comparing the measured density and the nominal density obtained from the rule of mixtures. The specific heat of the composite was estimated by means of the linear rule of mixtures using the specific heat for pure copper and 316L SS at the temperature of 50 °C.

2.4. Microhardness measurement

Vicker's microhardness (HV) was carried out on the cross-sections of the fusion zone for both coupons with a load of 500 gf and a dwell time of 15 s. A total of ten measurements were conducted for each

coupon. Measurement locations included three Cu-rich areas, three Fe-rich areas and four interfacial areas. Measurement locations were randomly selected within these areas.

3. Results and discussion

3.1. Post-heating versus heated-bed conversion of copper

Fig. 5 shows an optical micrograph of the cross-sectional microstructure of the fabricated 316L SS – Cu composite using (a) the post-heating and (b) the heated-bed method. Fig. 6a shows a higher magnification optical micrograph of a cross-sectional area within the microstructure of the heated-bed coupon. Distinct austenite and copper phases can be identified as gold and orange colors, respectively, due to the immiscibility of Cu within Fe. Further, Fig. 6b shows a continuous Cu phase which is important for increasing thermal conductivity through the elimination thermal interfaces [14, 30]. Irrespective of the conversion method, the microstructures clearly show the formation of stainless steel islands within continuous copper phases. Further, these micrographs also show that the post-heating coupon had several larger pores up to 60-70 µm in diameter while the heated-bed coupon had fewer, smaller pores.

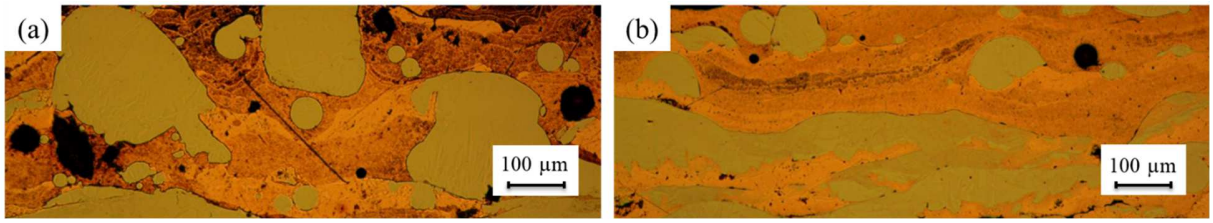

Fig. 5. (a) Cross-sectional optical microscope image of 316L SS – Cu composites fabricated using (a) the post-heating method and (b) the heated-bed method.

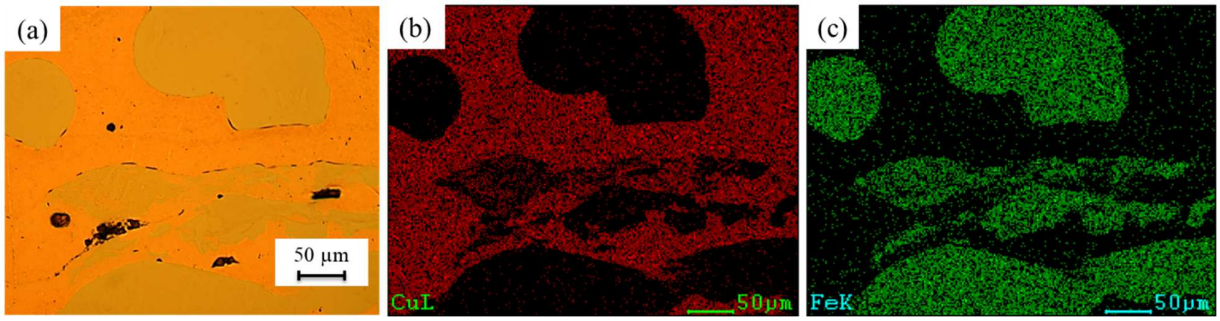

Fig. 6. (a) Optical microscope image of cross-section of the heated-bed coupon, (b and c) SEM-EDS elemental map of the coupon.

Since the EDS technique is not capable of quantifying the lighter elements in the coupons, a WDS analysis was performed. Fig. 7 shows a backscattered electron (BSE) image and elemental maps of the post-heating coupon obtained by WDS. The image shows a columnar SS morphology adjacent to two regions of copper; one with less oxygen (region A) and the other with more oxygen (region B). WDS analyses were performed on five randomly-selected areas within regions of less oxygen and more oxygen from each of the two coupons as well as an Fe-rich phase from the heated-bed coupon. The results are summarized in Table 3 and Fig. 8.

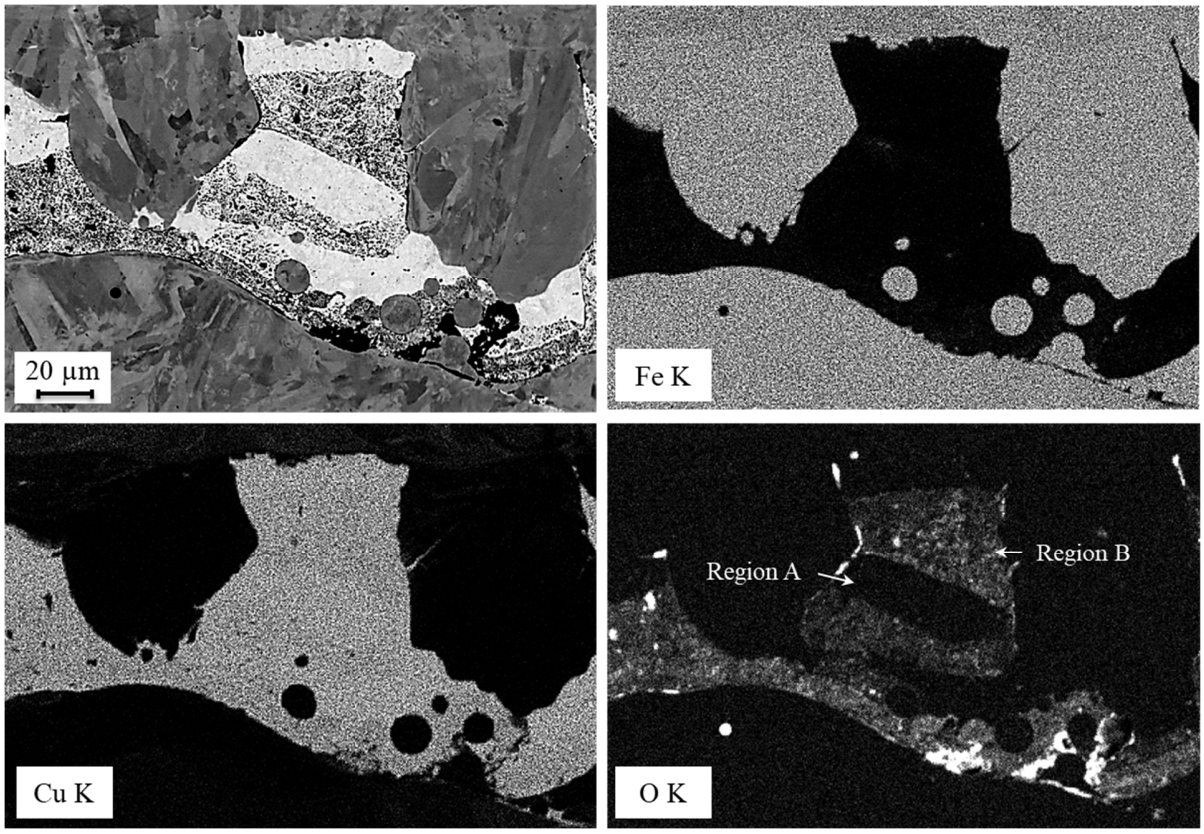

Fig. 7. BSE image (top left) and elemental maps (Fe, Cu, O) of the post-heating coupon obtained by WDS analysis.

Table 3. Average elemental composition (atomic %) of each Cu-rich and Fe-rich phases.

	Method	Cu	C	O	Fe	Ni	Cr	Mo	Mn	Si	S	P	Al
Cu-rich phase (Region A)	Post-heating	87.02 ± 0.67	5.48 ± 0.40	5.35 ± 0.25	0.29 ± 0.18	0.04 ± 0.04	0.06 ± 0.05	0.01 ± 0.01	0.01 ± 0.01	0.04 ± 0.01	0.02 ± 0.01	0.06 ± 0.01	1.62 ± 0.06
	Heated-bed	91.21 ± 2.05	3.85 ± 0.60	3.29 ± 0.53	0.83 ± 0.62	0.17 ± 0.13	0.32 ± 0.38	0.01 ± 0.01	0.03 ± 0.03	0.06 ± 0.07	0.04 ± 0.01	0.07 ± 0.01	0.13 ± 0.02
Cu-rich phase (Region B)	Post-heating	80.14 ± 3.52	6.67 ± 0.83	11.89 ± 2.88	0.22 ± 0.11	0.02 ± 0.02	0.07 ± 0.03	0.01 ± 0.01	0.01 ± 0.01	0.02 ± 0.02	0.01 ± 0.00	0.08 ± 0.00	0.85 ± 0.33
	Heated-bed	85.97 ± 2.48	5.16 ± 1.64	7.43 ± 1.49	0.70 ± 0.58	0.13 ± 0.09	0.25 ± 0.13	0.01 ± 0.01	0.04 ± 0.05	0.05 ± 0.02	0.01 ± 0.01	0.16 ± 0.04	0.18 ± 0.02
Fe-rich phase	Heated-bed	0.40 ± 0.02	2.36 ± 0.02	0.35 ± 0.24	66.96 ± 0.24	9.10 ± 0.28	18.15 ± 0.17	1.17 ± 0.04	0.96 ± 0.06	0.46 ± 0.02	0.00 ± 0.00	0.07 ± 0.01	0.03 ± 0.01

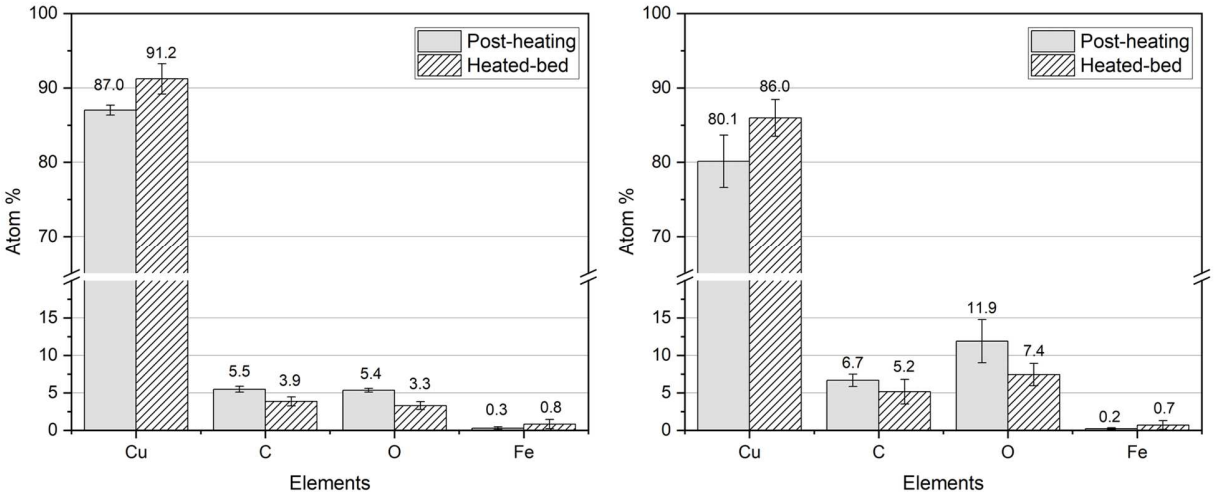

Fig. 8. Chemical element (atomic %) analysis of the converted Cu from (a) region A and (b) region B of post-heating and heated-bed coupons.

Based on the WDS analysis, it was found that the post-heating coupon has more impurities, such as carbon and oxygen in the converted Cu compared to the heated-bed coupon, leading to lower Cu wt% within the post-heating coupon. Pores and impurities like these are known to reduce thermal conductivity due to increased interfacial thermal resistance [31]. The reason for the heated-bed coupon having fewer pores and impurities is expected to be the result of 1) the flash evaporation and conversion of the ink droplets and 2) the incremental pipetting of the Cu ink into the pre-heated mold. It is expected that both reasons made it easier for the solvent and by-products to escape from the surface of the evolving Cu. Based on these results, the heated-bed method was chosen as the method for evaporating solvent and converting the Cu precursor going forward.

3.2. Interfacial cracks

Fig. 9 shows interfacial cracks observed throughout the heated-bed coupon between the two macrosegregated phases, which likely contributed to the low relative density of the sample. These cracks were observed within all coupons produced. These cracks likely reduced the effective thermal conductivity of the composite as a result of added interfacial thermal resistance [32]. The cracks are attributed to two main reasons as described below.

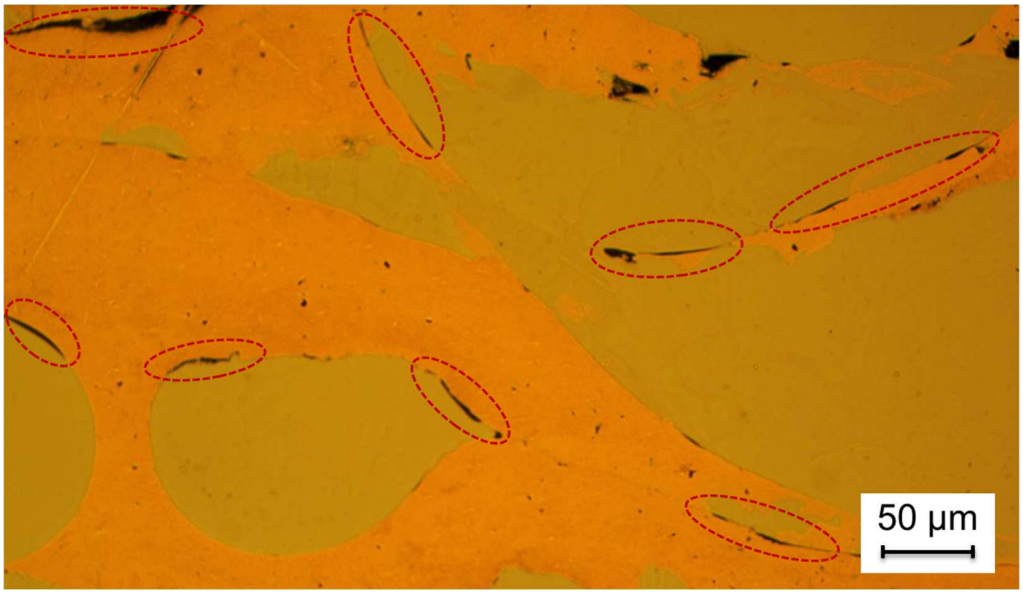

Fig. 9. Interfacial cracks observed at the interface between 316L SS and Cu phase.

First, Fig. 10 shows an interfacial crack found along a grain boundary between SS grains showing a cellular substructure. Cracking in the fabricated composite was likely caused by liquation cracking as a result of Cu liquation due to the wide difference in melting temperatures between Cu and 316L SS of about 315°C [33]. For the macrosegregated 316L SS–Cu composite, once the 316L SS solidifies, the remaining liquid Cu is bound to a constrained volume within the solidified SS. As the Cu solidifies, it experiences liquation cracking due to solidification shrinkage within a constrained volume. This cracking is likely further exacerbated by a coefficient of thermal expansion mismatch between the two phases [34], which would further place stress across the interface.

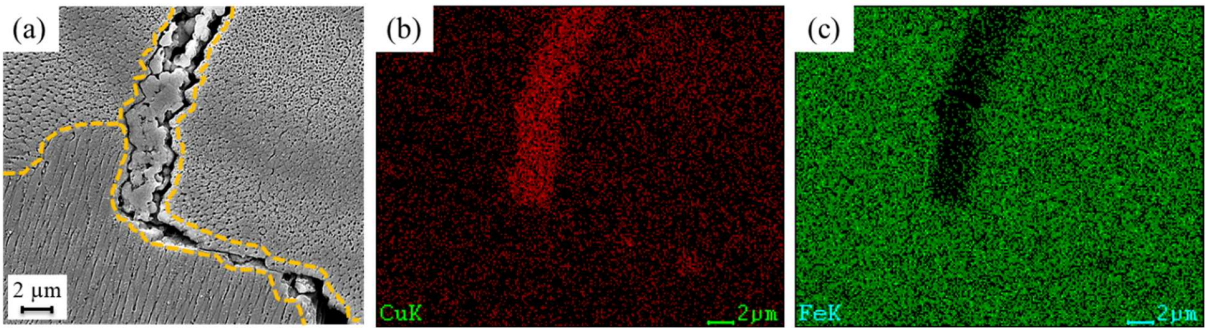

Fig. 10. (a) SEM image of cracks along the grain boundaries, (b and c) SEM-EDS elemental map of the coupon.

Second, investigation into some cracks provided evidence for the lack of fusion between Cu particles. Fig. 11 shows three regions at a macrosegregated interface: 1) a dense Cu region above the yellow dashed line; 2) a sintered Cu region just below the yellow dashed line and 3) an Fe-rich phase. According to Shin et al. [23], nano to micro-sized Cu particles are produced by the conversion of Cuf-AMP, similar to the sintered Cu shown in Fig. 11.

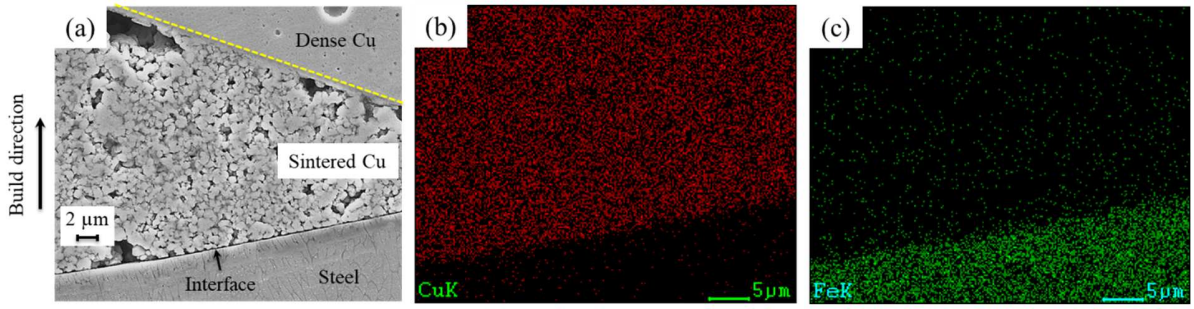

Fig. 11. (a) SEM image showing weak metallurgical bonding at the interface due to lack of fusion of Cu, (b and c) SEM-EDS elemental map of the coupon.

In contrast, Fig. 12 shows a macrosegregated interface with good bonding displaying submicrometer-sized Fe-rich phases in a Cu-rich continuous phase at the interface. This is attributed to the phenomenon of liquid separation from the steel phase and mixing due to convective forces in the laser melt pool [34]. Also, Fig. 13 shows good bonding at the interface with SS cellular substructures generally found in LPBF of 316L SS [35-37].

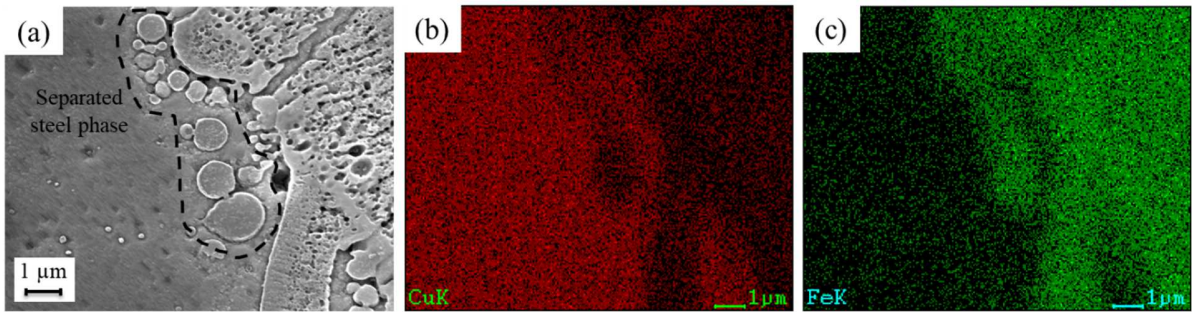

Fig. 12. (a) SEM image showing no cracking at the interface where separated steel phase diffused to Cu, (b and c) SEM-EDS elemental map of the coupon.

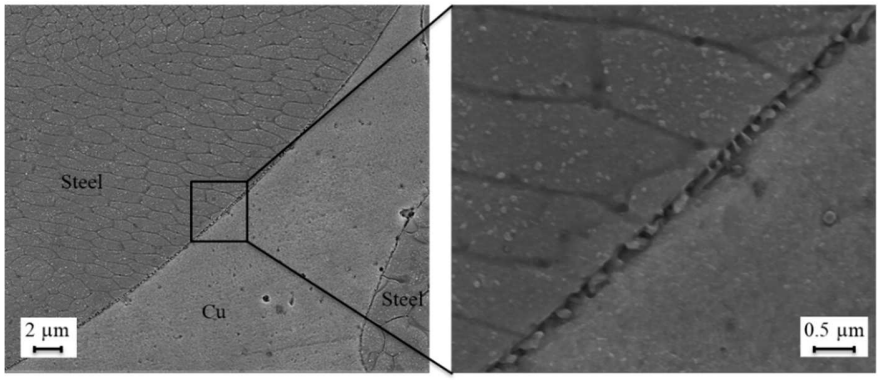

Fig. 13. Cellular substructure of the Fe-rich phase showing no cracking at the interface.

Future efforts are needed to investigate laser parameters to 1) increase the volumetric energy density to ensure full conversion and melting of copper; and 2) refine the grain size to provide higher yield strength

and better ductility due to Hall-Petch effects. Further, microstructural refinement will reduce thermal strains during solidification due to 1) the solidification of smaller volumes of liquid Cu; and 2) a coefficient of thermal expansion mismatch. To achieve this refinement, laser parameters would need to be adjusted to permit higher cooling rates [33].

3.3. Thermal conductivity

The effective thermal conductivity of the fabricated composite using the heated-bed method was found to be 41.0 W/m·K, which is an increase of 187% compared to 316L SS at the temperature of 50 °C. Since the laser parameters were not optimized, the relative density of the composite was found to be low. Given the high level of porosity with the composite sample, the measured thermal conductivity shows potential for greater enhancement through optimized parameters, since it is known that porosity adversely affects the thermal conductivity based on prior experimental studies [15, 38].

Table 4. Thermal properties and relative density of 316L SS – Cu composite and 316L SS.

At 50 °C	Thermal conductivity (W/m·K)	Thermal diffusivity (10^{-6} / m^2/s)	Specific heat (J/kg·K)	Density (10^3 / kg/m^3)	Relative density (%)
MMC	41.0	12.6	434.1	7.5	88.2
316L SS [39]	14.3	3.6	502.3	8.0	99.9

3.4. Microhardness

The microhardness on the cross-sections of the fusion zone was found to be 110 ± 61 HV and 123 ± 59, for the post-heating and heated-bed coupon, respectively, a decrease 45% and 39% compared to 200 HV of wrought annealed 316L SS [37], respectively. The larger pores of the post-heating coupon would likely contribute to decrease the microhardness compared to the heated-bed coupon.

4. Conclusions

A new method for producing a 316L SS–Cu composite with higher thermal conductivity compared to 316L SS was demonstrated using a jettable Cu ink. The composite was produced by depositing and converting the ink into Cu within a glovebox and then adding SS powder on top, which was then mixed and consolidated within a laser welder. Preliminary results show that a methanol-based Cuf-AMP ink can be decomposed to pure copper without the formation of copper oxide within an environment similar to that found within a LPBF process. A heated-bed method for ink deposition and conversion was found to produce microstructures with fewer pores and impurities compared with conventional post-heating methods. The effective thermal conductivity of the fabricated composite using the heated-bed method was measured to be 41.0 W/m·K which is 2.87 times that of 316L SS. Microhardness measurements for the heated-bed coupon were 123 ± 59 HV, which is a 39% decrease compared to wrought annealed 316L SS. The resulting composite was found to have a porosity of 12% caused primarily by voids and cracks at the interface between the SS-Cu phases. The cracks are expected to be the result of Cu liquation, thermal expansion mismatch and lack of fusion of converted Cu. Future efforts will investigate ways to decrease grain size and more fully melt and mix the SS and Cu phases as well as to investigate the mechanical properties of the composite.

Declaration of Competing Interest

The authors declare that they have no known competing financial interests or personal relationships that could have appeared to influence the work reported in this paper.

Acknowledgements

This work was supported by the Murdock Charitable Trust (contract #2016231), Department of Energy (DOE) (DE-EE0007888-10-4) Advanced Manufacturing Office (AMO) and the Rapid Advancement in Process Intensification Deployment (RAPID) Institute. We also gratefully acknowledge the OSU Electron Microscopy Facility and the Advanced Technology and Manufacturing Institute (ATAMI) staff. The authors also thank Dr. Mas Subramanian and Dr. Li for allowing us to use the LFA 457 tool to measure the thermal diffusivity of the composite.

References

[1] S. Catchpole-Smith, R. Sélo, A. Davis, I. Ashcroft, C. Tuck, A. Clare, Thermal conductivity of TPMS lattice structures manufactured via laser powder bed fusion, Additive Manufacturing 30 (2019) 100846.
[2] J.-H. You, K. Park, Design and additive manufacturing of thermal metamaterial with high thermal resistance and cooling capability, Additive Manufacturing 41 (2021) 101947.
[3] S. Narayana, Y. Sato, Heat flux manipulation with engineered thermal materials, Physical review letters 108(21) (2012) 214303.
[4] E.M. Dede, T. Nomura, P. Schmalenberg, J. Seung Lee, Heat flux cloaking, focusing, and reversal in ultra-thin composites considering conduction-convection effects, Applied Physics Letters 103(6) (2013) 063501.
[5] T. Han, X. Bai, J.T. Thong, B. Li, C.W. Qiu, Full control and manipulation of heat signatures: cloaking, camouflage and thermal metamaterials, Advanced Materials 26(11) (2014) 1731-1734.
[6] T. Han, X. Bai, D. Gao, J.T. Thong, B. Li, C.-W. Qiu, Experimental demonstration of a bilayer thermal cloak, Physical review letters 112(5) (2014) 054302.
[7] H. Xu, X. Shi, F. Gao, H. Sun, B. Zhang, Ultrathin three-dimensional thermal cloak, Physical Review Letters 112(5) (2014) 054301.
[8] Y. Li, X. Shen, Z. Wu, J. Huang, Y. Chen, Y. Ni, J. Huang, Temperature-dependent transformation thermotics: from switchable thermal cloaks to macroscopic thermal diodes, Physical review letters 115(19) (2015) 195503.
[9] S.Y. Kim, J.-M. Koo, A.V. Kuznetsov, Effect of anisotropy in permeability and effective thermal conductivity on thermal performance of an aluminum foam heat sink, Numerical Heat Transfer: Part A: Applications 40(1) (2001) 21-36.
[10] S. Baek, C. Lee, S. Jeong, Effect of flow maldistribution and axial conduction on compact microchannel heat exchanger, Cryogenics 60 (2014) 49-61.
[11] P. Kroeger, Performance deterioration in high effectiveness heat exchangers due to axial heat conduction effects, Advances in cryogenic engineering, Springer1967, pp. 363-372.
[12] C. Xue, J. Yu, Enhanced thermal conductivity in diamond/aluminum composites: comparison between the methods of adding Ti into Al matrix and coating Ti onto diamond surface, Surface and Coatings Technology 217 (2013) 46-50.
[13] P. Ruch, O. Beffort, S. Kleiner, L. Weber, P.J. Uggowitzer, Selective interfacial bonding in Al (Si)–diamond composites and its effect on thermal conductivity, Composites science and technology 66(15) (2006) 2677-2685.
[14] C.V. Ugarteche, K.P. Furlan, R.d.V. Pereira, G. Trindade, R. Binder, C. Binder, A.N. Klein, Effect of microstructure on the thermal properties of sintered iron-copper composites, Materials Research 18(6) (2015) 1176-1182.
[15] S.H. Lee, S.Y. Kwon, H.J. Ham, Thermal conductivity of tungsten–copper composites, Thermochimica acta 542 (2012) 2-5.

[16] C. Kenel, G. Dasargyri, T. Bauer, A. Colella, A.B. Spierings, C. Leinenbach, K. Wegener, Selective laser melting of an oxide dispersion strengthened (ODS) γ-TiAl alloy towards production of complex structures, Materials and Design 134 (2017) 81-90.
[17] M. Ghayoor, K. Lee, Y. He, C.-h. Chang, B.K. Paul, S. Pasebani, Selective laser melting of austenitic oxide dispersion strengthened steel: Processing, microstructural evolution and strengthening mechanisms, Materials Science and Engineering: A (2020) 139532.
[18] M. Ghayoor, S. Mirzababaei, A. Sittiho, I. Charit, B.K. Paul, S. Pasebani, Thermal stability of additively manufactured austenitic 304L ODS alloy, Journal of Materials Science & Technology 83 (2021) 208-218.
[19] B.K. Paul, K. Lee, Y. He, M. Ghayoor, C.-h. Chang, S. Pasebani, Oxide dispersion strengthened 304 L stainless steel produced by ink jetting and laser powder bed fusion, CIRP Annals (2020).
[20] W. Li, Q. Sun, L. Li, J. Jiu, X.-Y. Liu, M. Kanehara, T. Minari, K. Suganuma, The rise of conductive copper inks: challenges and perspectives, Applied Materials Today 18 (2020) 100451.
[21] D. Tomotoshi, H. Kawasaki, Surface and interface designs in copper-based conductive inks for printed/flexible electronics, Nanomaterials 10(9) (2020) 1689.
[22] W. Yang, E.J. List-Kratochvil, C. Wang, Metal particle-free inks for printed flexible electronics, Journal of Materials Chemistry C 7(48) (2019) 15098-15117.
[23] D.-H. Shin, S. Woo, H. Yem, M. Cha, S. Cho, M. Kang, S. Jeong, Y. Kim, K. Kang, Y. Piao, A Self-Reducible and Alcohol-Soluble Copper-Based Metal–Organic Decomposition Ink for Printed Electronics, ACS Applied Materials & Interfaces 6(5) (2014) 3312-3319.
[24] Y. Farraj, M. Grouchko, S. Magdassi, Self-reduction of a copper complex MOD ink for inkjet printing conductive patterns on plastics, Chemical Communications 51(9) (2015) 1587-1590.
[25] S. Babar, E. Mohimi, B. Trinh, G.S. Girolami, J.R. Abelson, Surface-selective chemical vapor deposition of copper films through the use of a molecular inhibitor, ECS Journal of Solid State Science and Technology 4(7) (2015) N60.
[26] A. Gelatos, R. Marsh, M. Kottke, C. Mogab, Chemical vapor deposition of copper from Cu+ 1 precursors in the presence of water vapor, Applied physics letters 63(20) (1993) 2842-2844.
[27] G.G. Rozenberg, E. Bresler, S.P. Speakman, C. Jeynes, J.H.G. Steinke, Patterned low temperature copper-rich deposits using inkjet printing, Applied Physics Letters 81(27) (2002) 5249-5251.
[28] W. Xu, T. Wang, Synergetic effect of blended alkylamines for copper complex ink to form conductive copper films, Langmuir 33(1) (2017) 82-90.
[29] J. Pouchou, F. Pichoir, PAP correction procedure for improved quantitative microanalysis, San Francisco Press San Francisco, CA, 1984, pp. 104-106.
[30] J. Wang, J.K. Carson, M.F. North, D.J. Cleland, A new structural model of effective thermal conductivity for heterogeneous materials with co-continuous phases, International journal of heat and mass transfer 51(9-10) (2008) 2389-2397.
[31] R.P. Minneci, E.A. Lass, J.R. Bunn, H. Choo, C.J. Rawn, Copper-based alloys for structural high-heat-flux applications: a review of development, properties, and performance of Cu-rich Cu–Cr–Nb alloys, International Materials Reviews (2020) 1-32.
[32] R. Rurali, X. Cartoixà, L. Colombo, Heat transport across a SiGe nanowire axial junction: Interface thermal resistance and thermal rectification, Physical Review B 90(4) (2014) 041408.
[33] S. Kou, Welding metallurgy, New Jersey, USA (2003) 431-446.
[34] Z. Liu, D. Zhang, S. Sing, C. Chua, L. Loh, Interfacial characterization of SLM parts in multi-material processing: Metallurgical diffusion between 316L stainless steel and C18400 copper alloy, Materials Characterization 94 (2014) 116-125.
[35] F. Vecchiato, H. De Winton, P. Hooper, M. Wenman, Melt pool microstructure and morphology from single exposures in laser powder bed fusion of 316L stainless steel, Additive Manufacturing 36 (2020) 101401.

[36] X. Wang, J.A. Muniz-Lerma, O. Sánchez-Mata, M.A. Shandiz, M. Brochu, Microstructure and mechanical properties of stainless steel 316L vertical struts manufactured by laser powder bed fusion process, Materials Science and Engineering: A 736 (2018) 27-40.
[37] T. Kurzynowski, K. Gruber, W. Stopyra, B. Kuźnicka, E. Chlebus, Correlation between process parameters, microstructure and properties of 316 L stainless steel processed by selective laser melting, Materials Science and Engineering: A 718 (2018) 64-73.
[38] J.C. Simmons, X. Chen, A. Azizi, M.A. Daeumer, P.Y. Zavalij, G. Zhou, S.N. Schiffres, Influence of processing and microstructure on the local and bulk thermal conductivity of selective laser melted 316L stainless steel, Additive Manufacturing 32 (2020) 100996.
[39] C.S. Kim, Thermophysical properties of stainless steels, Argonne National Lab., Ill.(USA), 1975.